Article

Chinese Science Bulletin

Progress of Projects Supported by NSFC
Explosion Mechanics

April 2013 Vol.58 No.11: 1216–1227
doi: 10.1007/s11434-013-5766-6

Additive Runge-Kutta methods for $H_2/O_2/Ar$ detonation with a detailed elementary chemical reaction model

LI Jian, REN HuiLan* & NING JianGuo

State Key Laboratory of Explosion Science and Technology, Beijing Institute of Technology, Beijing 100081, China

Received January 9, 2013; accepted February 17, 2013

We report here the additive Runge-Kutta methods for computing reactive Euler equations with a stiff source term, and in particular, their applications in gaseous detonation simulations. The source term in gaseous detonation is stiff due to the presence of wide range of time scales during thermal-chemical non-equilibrium reactive processes and some of these time scales are much smaller than that of hydrodynamic flow. The high order, L-stable, additive Runge-Kutta methods proposed in this paper resolved the stiff source term into the stiff part and non-stiff part, in which the stiff part was solved implicitly while the non-stiff part was handled explicitly. The proposed method was successfully applied to simulating the gaseous detonation in a stoichiometric $H_2/O_2/Ar$ mixture based on a detailed elementary chemical reaction model comprised of 9 species and 19 elementary reactions. The results showed that the stiffly accurate additive Runge-Kutta methods can capture the discontinuity well, and describe the detonation complex wave configurations accurately such as the triple wave structure and cellular pattern.

source term, additive Runge-Kutta methods, stiffness, gaseous detonation

Citation: Li J, Ren H L, Ning J G. Additive Runge-Kutta methods for $H_2/O_2/Ar$ detonation with a detailed elementary chemical reaction model. Chin Sci Bull, 2013, 58: 1216–1227, doi: 10.1007/s11434-013-5766-6

Reacting flows, specifically in gaseous combustion, have been a significant topic of active research for more than one hundred years. The strong coupling between hydrodynamic flow and chemical kinetics is complex and even today many phenomena are not very well understood yet. Gaseous detonation is a process of supersonic combustion in which a shock wave is propagated and supported by the energy release in a reaction zone behind it. It is the more powerful and destructive of the two general classes of combustion, the other one being deflagration.

The primary difficulty in computing reacting flows is the source term stiffness inherent in the reactive Euler equations in temporal integrations. Besides, the viscous stress and heat flux terms in the boundary layers can cause the stiffness too. The source terms are stiff because the thermal-chemical non-equilibrium reactive processes possess a wide range of time scales and some of them are much smaller than that of hydrodynamic flow [1]. The simulation will be inefficient when the explicit methods rather than the implicit methods are used, because the time-step sizes dictated by the stability restraint in explicit methods are much smaller than those required by the CFL condition. Due to these limitations in explicit methods, the implicit methods are normally required to simulate gaseous detonation. The practical implicit methods for gaseous detonation simulation can be categorized into two classes, i.e. the time-splitting method and the additive semi-implicit method [2,3].

The time-splitting methods [4–8], resolve the source term of reactive Euler equations into

$$\boldsymbol{U}_t = \boldsymbol{L}(\boldsymbol{U}) + \boldsymbol{S}(\boldsymbol{U}), \tag{1}$$

where $\boldsymbol{L}(\boldsymbol{U})$, $\boldsymbol{S}(\boldsymbol{U})$ are the convective term and reactive source term, respectively. The contribution from the convective term is first calculated to get an intermediate value $\tilde{\boldsymbol{U}}^{n+1}$, the source term contributions are evaluated to give $\boldsymbol{U}^{n+1}$ in the next step [9]. The additive semi-implicit meth-

*Corresponding author (email: huilanren@bit.edu.cn)

ods resolve ODEs into the stiff part and non-stiff part, in which the stiff part is computed implicitly while the non-stiff part explicitly. Zhong [1] conducted a detailed study on additive semi-implicit methods and proposed a stiff accurate semi-implicit Runge-Kutta method up to the third order. The proposed methods had been applied in reactive flow computation. Meanwhile, Kennedy and Carpenter [10] constructed an L-stable, stiffly accurate ARK_2 method for solving spatially discretized one-dimensional convection-diffusion-reaction (CDR) equations. Their method has been combined with local discontinuous Galerkin methods by Xia and Wang [11,12] in studying PDEs.

The main objective of this paper is to conduct a numerical study of the gaseous detonation in one-dimensional and two-dimensional tubes using high resolution WENO scheme and additive Runge-Kutta methods with the numerical accuracies ranging from the third to fifth order. A detailed chemical kinetics model comprised of 9 species and 19 elementary reactions was employed for a stoichiometric oxygen-hydrogen mixture diluted with argon. The results were compared with those obtained by the explicit methods.

1 Governing equation and numerical methods

1.1 Governing equation

The governing equations for gaseous detonation are the reactive Euler equations of multi-species in which the viscosity, the heat transfer, the diffusion and body forces are neglected:

$$\boldsymbol{U}_t + \left[\boldsymbol{F}(\boldsymbol{U})\right]_x + \left[\boldsymbol{G}(\boldsymbol{U})\right]_y = \boldsymbol{S}, \tag{2}$$

$$\boldsymbol{U} = \begin{pmatrix} \rho \\ \rho u \\ \rho v \\ E \\ \rho Y_1 \\ \vdots \\ \rho Y_N \end{pmatrix}, \ \boldsymbol{F}(\boldsymbol{U}) = \begin{pmatrix} \rho u \\ \rho u^2 + p \\ \rho uv \\ (E+p)u \\ \rho u Y_1 \\ \vdots \\ \rho u Y_N \end{pmatrix}, \ \boldsymbol{G}(\boldsymbol{U}) = \begin{pmatrix} \rho v \\ \rho uv \\ \rho v^2 + p \\ (E+p)v \\ \rho v Y_1 \\ \vdots \\ \rho v Y_N \end{pmatrix}, \tag{3}$$

$$\boldsymbol{S} = \begin{pmatrix} 0 \\ 0 \\ 0 \\ 0 \\ \omega_1(T,\rho,Y_1,Y_2,\ldots Y_N) \\ \vdots \\ \omega_N(T,\rho,Y_1,Y_2,\ldots Y_N) \end{pmatrix},$$

$$E = \rho h - p + \rho u^2/2, \tag{4}$$

$$h = e + p/\rho, \tag{5}$$

where ω_i is the mass production rate of the i-th species, ρ is the density, u and v are velocities, E is the energy per unit volume, e, p and h are the internal energy, the pressure, and the enthalpy per unit mass, respectively. N is the number of different species being considered, and Y_i is the mass fraction of the i-th species (note that $Y_N = 1 - \sum_{i=1}^{N-1} Y_i$), and $\boldsymbol{S}$ represents the stiff reactive source term.

The internal energy, the enthalpy, and the specific heat capacities for a perfect gas are functions of the temperature only. Under such circumstances, we can write

$$h_i = h_i(T), \quad e_i = e_i(T), \quad c_{pi} = c_{pi}(T), \quad c_{vi} = c_{vi}(T),$$

$$h = \sum_{i=1}^{N} Y_i h_i, \ e = \sum_{i=1}^{N} Y_i e_i, \ c_p = \sum_{i=1}^{N} Y_i c_{pi}, \ c_v = \sum_{i=1}^{N} Y_i c_{vi}, \tag{6}$$

in which c_{pi} and c_{vi} are the specific heat capacities of the i-th species at constant pressure and volume, respectively. The enthalpy and internal energy of a perfect gas are related to its heat capacities by

$$\mathrm{d}h_i(T) = c_{pi}(T)\mathrm{d}T, \ \mathrm{d}e_i(T) = c_{vi}(T)\mathrm{d}T, \tag{7}$$

$$h_i = h_i(0) + \int_0^T c_{pi}(s)\mathrm{d}s. \tag{8}$$

The perfect gases can be further divided into two categories, i.e. the thermally perfect gas in which the specific heat capacities are the functions of temperature, and the calorically perfect gas whose specific heat capacities are constant [13]. Accordingly, eq. (8) can be simplified for a calorically perfect gas:

$$h_i = h_i^f + c_{pi}T, h = c_p T, \tag{9}$$

where h_i^f is the enthalpy per unit mass at 0 K for the i-th species. The state equation of the calorically perfect gas can be obtained by substituting eq. (9) and $c_p = \gamma R/(\gamma - 1)$ into eq. (4):

$$E = \frac{p}{\gamma - 1} + \frac{1}{2}\rho\left(u^2 + v^2\right). \tag{10}$$

Particularly, if all the species are thermally perfect, we have

$$\frac{c_{pi}}{R_i} = \sum_{k=1}^{5} a_{ki} T^{k-1}, \ \frac{h_i}{R_i T} = \sum_{k=1}^{5} \frac{a_{ki} T^{k-1}}{k} + \frac{a_{6i}}{T}, \tag{11}$$

in which R_i is the gas constant of the i-th species and $R = \sum_{i=1}^{N} Y_i R_i$. The values of a_{1i}, a_{2i},…a_{6i} are taken from JANAF tables [14].

1.2 Detailed chemical kinetics model

A detailed chemical model comprised of 9 species and 19

elementary reactions was employed here for describing hydrogen-oxygen-argon detonation [15], which was choose because of its computation efficiency and accuracy comparing to other models, as shown in Table 1. The chemical reactions can be expressed as

$$\sum_{i=1}^{9} v'_{ik} x_i \underset{K_{b,k}}{\overset{K_{f,k}}{\rightleftharpoons}} \sum_{i=1}^{9} v''_{ik} x_i, \quad k=1, 2, 3,\ldots 19, \tag{12}$$

in which v'_{ik} and v''_{ik} are the chemical stoichiometric coefficients of the i-th species in the k-th reaction, x_i is the mole fraction of the i-th species, and $K_{f,k}(K_{b,k})$ are the forward (backward) reaction rate constants of the k-th reaction, respectively. $K_{f,k}$ and $K_{b,k}$ follow the Arrhenius law and satisfy the chemical equilibrium conditions:

$$\begin{aligned} K_{f,k} &= A_k T^{nk} \exp\left(-E_{ak}/RT\right), \\ K_{b,k} &= K_{f,k}/K_{c,k}, \\ K_{c,k} &= K_{p,k}\left(p_{\text{atm}}/RT\right)^{\sum_{i=1}^{9}\left(v''_{ik}-v'_{ik}\right)}, \\ K_{p,k} &= \exp\left[\sum_{i=1}^{9}\left\{\left(v''_{ik}-v'_{ik}\right)\left(\frac{s_i^o}{R_i}-\frac{h_i}{R_i T}\right)\right\}\right], \end{aligned} \tag{13}$$

where $R_i=R_u/W_i$, R_u is the universal gas constant, p_{atm} is the atmospheric pressure, s_i^o is the entropy at the standard state, A_k is the pre-exponential constant, n_k is the temperature power, and E_{ak} is the activation energy. The finite production rate ω_i for the i-th specie is calculated under the assumption that all involved reactions are elementary reactions:

$$\begin{aligned} &\omega_i \\ &= W_i \sum_{k=1}^{19}\left(v''_{ik}-v'_{ik}\right)\left\{\sum_{i=1}^{9}\alpha_{ik}C_{xi}\right\}\left\{K_{f,k}\prod_{i=1}^{9}\left(C_{xi}\right)^{v'_{ik}} - K_{b,k}\prod_{i=1}^{9}\left(C_{xi}\right)^{v''_{ik}}\right\}, \end{aligned} \tag{14}$$

where W_i and C_{xi} are the molecular weight and the molar concentration of i-th species ($C_{xi}=\rho_i/W_i$), respectively, and α_{ik} represents the third body coefficients for the i-th species and k-th equations. For hydrogen and oxygen, $\alpha_{1k}=2.5(H_2)$ and $\alpha_{8k}=16(H_2O)$, respectively, while $\alpha_{ik}=0$ for all other species.

1.3 Numerical methods

Considering the stiffness of the reactive source terms, the additive Runge-Kutta (ARK_N) method is adopted in this work to couple the Euler equations to the chemical reactions. Following the work [16,17], ARK_N methods can be used to solve the equations of the form:

$$\mathrm{d}U/\mathrm{d}t = F(U) = \sum_{\nu=1}^{N} F^{[\nu]}(U), \tag{15}$$

Table 1 Reaction mechanism and some related parameters (cm^3 mol s cal)

		A_k	n_k	E_{ak}
1	$H+O_2\leftrightarrow O+OH$	6.00×10^{14}	0.0	16790
2	$O+H_2\leftrightarrow H+OH$	1.07×10^{4}	2.80	5921
3	$OH+H_2\leftrightarrow H+H_2O$	7.00×10^{12}	0.0	4400
4	$O+H_2O\leftrightarrow OH+OH$	1.50×10^{10}	1.14	17190
5	$H_2+M\leftrightarrow H+H+M$	2.90×10^{18}	–1.0	104330
6	$O+O+M\leftrightarrow O_2+M$	6.17×10^{15}	–0.5	0.0
7	$O+H+M\leftrightarrow OH+M$	1.00×10^{15}	0.0	–497
8	$H+OH+M\leftrightarrow H_2O+M$	8.80×10^{21}	–2.0	0.0
9	$H+O_2+M\leftrightarrow HO_2+M$	6.76×10^{19}	–1.42	0.0
10	$HO_2+H\leftrightarrow H_2+O_2$	2.50×10^{13}	0.0	693
11	$HO_2+H\leftrightarrow OH+OH$	2.51×10^{13}	0.0	1910
12	$HO_2+O\leftrightarrow OH+O_2$	2.00×10^{13}	0.0	0.0
13	$HO_2+OH\leftrightarrow H_2O+O_2$	1.20×10^{13}	0.0	0.0
14	$HO_2+HO_2\leftrightarrow H_2O_2+O_2$	1.82×10^{12}	0.0	0.0
15	$H_2O_2+M\leftrightarrow OH+OH+M$	3.19×10^{17}	0.0	47100
16	$H_2O_2+H\leftrightarrow H_2O+OH$	3.20×10^{14}	0.0	9000
17	$H_2O_2+H\leftrightarrow H_2+HO_2$	4.79×10^{13}	0.0	7950
18	$H_2O_2+O\leftrightarrow OH+HO_2$	9.54×10^{6}	2.0	3970
19	$H_2O_2+OH\leftrightarrow H_2O+HO_2$	1.00×10^{13}	0.0	1800

where $F(U)$ can be resolved into N terms. For reactive Euler equation, N=2, i.e. the convective term and reactive source term. Each time step in ARK$_N$ is calculated by

$$U^{(i)} = U^{(n)} + (\Delta t)\sum_{v=1}^{N}\sum_{j=1}^{s} a_{ij}^{[v]} F^{[v]}(U^{(j)}), \tag{16}$$

$$U^{(n+1)} = U^{(n)} + (\Delta t)\sum_{v=1}^{N}\sum_{j=1}^{s} b_{i}^{[v]} F^{[v]}(U^{(j)}), \tag{17}$$

where each of the N terms is integrated by its own s-stage Runge-Kutta method. The Butcher coefficients $a_{ij}^{[v]}$ and $b_i^{[v]}$, v=1,2,$\cdots N$, are constrained, at a minimum, by some accuracy and stability considerations. For a detailed description of the methods as well as their implementation and applications, we refer the readers to [10]. Eq. (16) is implicit, so Newton-raphson method was used to solve it.

The reactive equation in ARK$_2$ methods can be written as

$$U_t = F_{ns} + F_s, \tag{18}$$

where F_{ns} and F_s represent the non-stiff and stiff terms, respectively. The implicit-explicit ARK$_2$ methods are particularly attractive, in which the explicit Runge-Kutta (ERK) schemes are combined with stiffly accurate, explicit, singly diagonally implicit Runge-Kutta (ESDIRK) schemes. ERK methods are utilized to integrate the non-stiff terms, while the stiff terms are handled using ESDIRK methods [18,19]. The coefficients for the ERK and ESDIRK methods are denoted by $a_{ij}^{[E]}$ and $a_{ij}^{[I]}$ in the remaining parts of this paper, respectively. ESDIRKs offer the advantages of allowing L-stability, stiff accuracy, and a second order accuracy. They differ from the traditional SDIRK [20,21] methods by having an explicit first stage. ARK3(2)4L[2]SA, ARK4(3)6L[2]SA and ARK5(4)8L[2]SA[5] that adopted in this work are third-order, fourth-order, and fifth-order ARK2 methods, respectively. Meanwhile, the non-stiff convective term in this paper was numerically discretized in space using fifth-order WENO scheme [22–29].

1.4 Initial and boundary conditions

The numerical simulation was conducted to simulate a detonation wave propagating in a square chamber with a stoichiometric H_2/O_2 mixture diluted with 70% argon. The initial pressure and temperature were 6670 Pa and 298 K, respectively. The solution of one-dimensional steady ZND detonation wave with a strong density perturbation ahead was placed on a two-dimensional mesh serving as the initial conditions for the two-dimensional simulation (Figure 1). Neumann boundary conditions were imposed on the inlet and outlet, and reflected boundary conditions were applied on the upper and lower walls. For one-dimensional detonation, a proportion of pre-mixed gas was enclosed at the left end, and then the direction initiation was employed to generate the detonation waves.

2 Test problems

2.1 Convective-reactive equations

The temporal accuracies of ARK3(2)4L[2]SA, ARK4(3)6L[2]SA and ARK5(4)8L[2]SA[5] were evaluated by solving the convective-reactive equation:

$$u_t + u_x = \varepsilon u, \quad 0 \leqslant x \leqslant 1, \quad u(0,x) = \sin(2\pi x), \quad \text{periodic boundary condition.} \tag{19}$$

Eq. (19) exhibits an increasing stiffness as $\varepsilon \to 0$. In the IMEX formulation, the εu term was integrated implicitly while all other terms were integrated explicitly. The initial boundary value problem of eq. (19) had a smooth exact solution:

$$u(t,x) = e^{\varepsilon t}\sin\left(2\pi\left(x-t\right)\right). \tag{20}$$

The temporal accuracies of the ARK2 methods were evaluated through a grid refinement study in which the computations were conducted successively with a time step half of that used in the previous computation. The same spatial

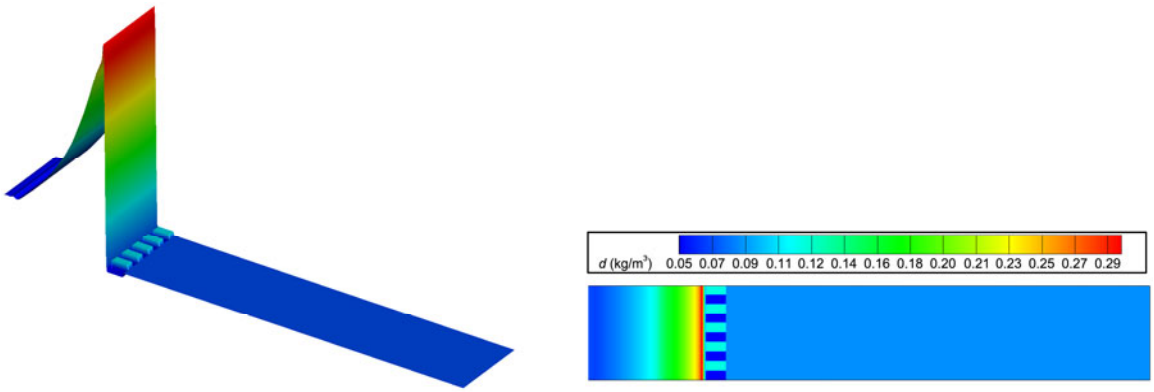

Figure 1 Initial condition for 2-D gaseous detonation in a channel (density).

grid was used for all the test computations to prevent the spatial discretization error changing. The order of temporal accuracy was determined numerically by computing the parameter R_p defined by (ε=0.1):

$$e_h = |u_0 - u_h|, \quad R_p = 2^p = \sqrt{e_h / e_{h/2}}, \tag{21}$$

in which p is the order of temporal accuracy, e_h is the numerical error, u_0 and u_h are the exact solution and the numerical solution computed using time step h, respectively. The results are shown in Table 2. As shown in Table 2, the ARK5(4)8L[2]SA[5], ARK4(3)6L[2]SA and ARK3(2)4L[2]SA methods were fifth-order, fourth-order and third-order, respectively.

The changes in computation errors were plotted against ε in Figure 2. For IMEX ARK3(2)4L[2]SA, third-order TVD Runge-Kutta (reference, Shu), three steps third-order SSPRK (reference, Ruuth) and eight steps third-order SSPRK (reference, Ruuth). It can be seen that the computation errors of all four schemes were roughly the same for ε<10, while ARK3(2)4L[2]SA exhibited the smallest errors for ε>10.

2.2 Shock tube problems

The proposed method has been tested by computing two classic Shock tube problems, i.e. the Sod and Lax-Harten shock tube problems. The computations were conducted on a mesh of 200 cells. The initial conditions were

$$\text{Sod}\begin{cases}\rho = 1.000,\ u = 0.0,\ p = 1.0, & 0 \leqslant x < 0.5,\\ \rho = 0.125,\ u = 0.0,\ p = 0.1, & 0.5 \leqslant x \leqslant 1.\end{cases} \tag{22}$$

$$\text{Lax}\begin{cases}\rho = 0.445,\ u = 0.7,\ p = 3.52773, & 0 \leqslant x < 0.5,\\ \rho = 0.500,\ u = 0.0,\ p = 0.57100, & 0.5 \leqslant x \leqslant 1.\end{cases} \tag{23}$$

The partial differential equations (PDE) in Sod and Lax-Harten shock tube problems are derived based on the conservation laws. The initial value problem of these PDEs is a Riemann problem. The Riemann problem is one of the standard verification problems for testing numerical algorithms. The computed density, the velocity and the pressure profiles are shown in Figure 4 along with those from the exact solution. It is clearly evident that the computation results are in good agreement with the exact solution.

2.3 Constant volume explosion model

The constant volume explosion model can be expressed either as the differential species conservation equations subject to algebraic physical constraints or as a set of purely differential equations. The algebraic-differential equations correspond to the Lagrangian conservation equations for each species:

$$\frac{\mathrm{d}Y_i}{\mathrm{d}t} = \frac{1}{\rho}\omega_i,\ \frac{\mathrm{d}T}{\mathrm{d}t} = -\frac{1}{c_v}\sum_{i=1}^{9} e_i\omega_i,\ \frac{\mathrm{d}\rho}{\mathrm{d}t} = 0, \tag{24}$$

Table 2 Temporal accuracy test for third-order ARK3(2)4L[2]SA, fourth-order ARK4(3)6L[2]SA, ARK5(4)8L[2]SA (x=0.5, t=0.2)

Δt	Err1	R_p	Order	Err2	R_p	Order	Err3	R_p	Order
h=0.04	1.82×10^{-3}	7.2	2.85	3.21×10^{-4}	13.0	3.70	5.57×10^{-5}	26.0	4.70
h/2	2.53×10^{-4}	7.7	2.94	2.47×10^{-5}	15.1	3.92	2.14×10^{-6}	28.8	4.85
h/4	3.29×10^{-5}	7.9	2.98	1.63×10^{-6}	15.9	3.99	7.43×10^{-8}	29.9	4.90
h/8	4.16×10^{-6}	8.0	3.00	1.03×10^{-7}	16.1	4.01	2.49×10^{-9}	32.7	5.03
h/16	5.21×10^{-7}	8.2	3.04	6.37×10^{-9}	16.6	4.05	7.62×10^{-11}	33.1	5.05
h/32	6.43×10^{-8}	–	–	3.85×10^{-10}	–	–	2.30×10^{-12}	–	–

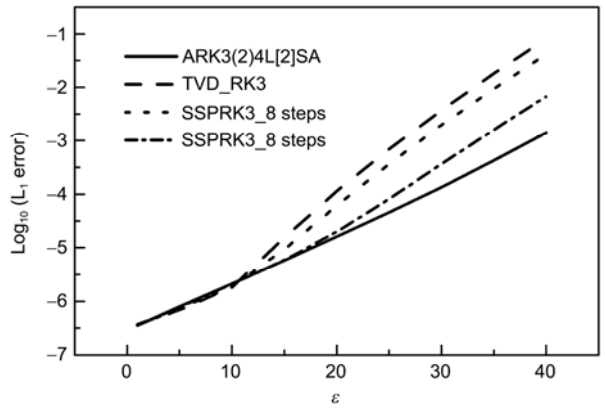

Figure 2 Error versus stiffness parameters ε for four third-order schemes.

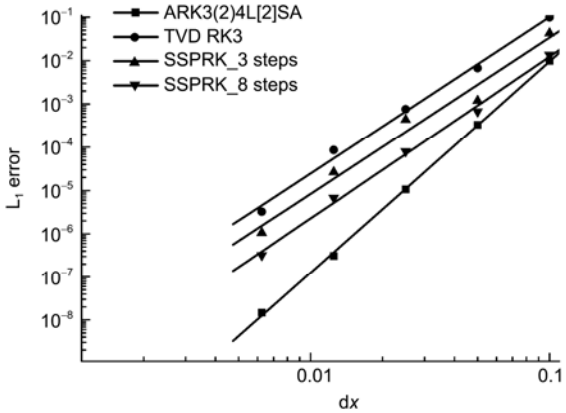

Figure 3 Grid convergence study for four third-order schemes with stiffness parameters ε=0.1.

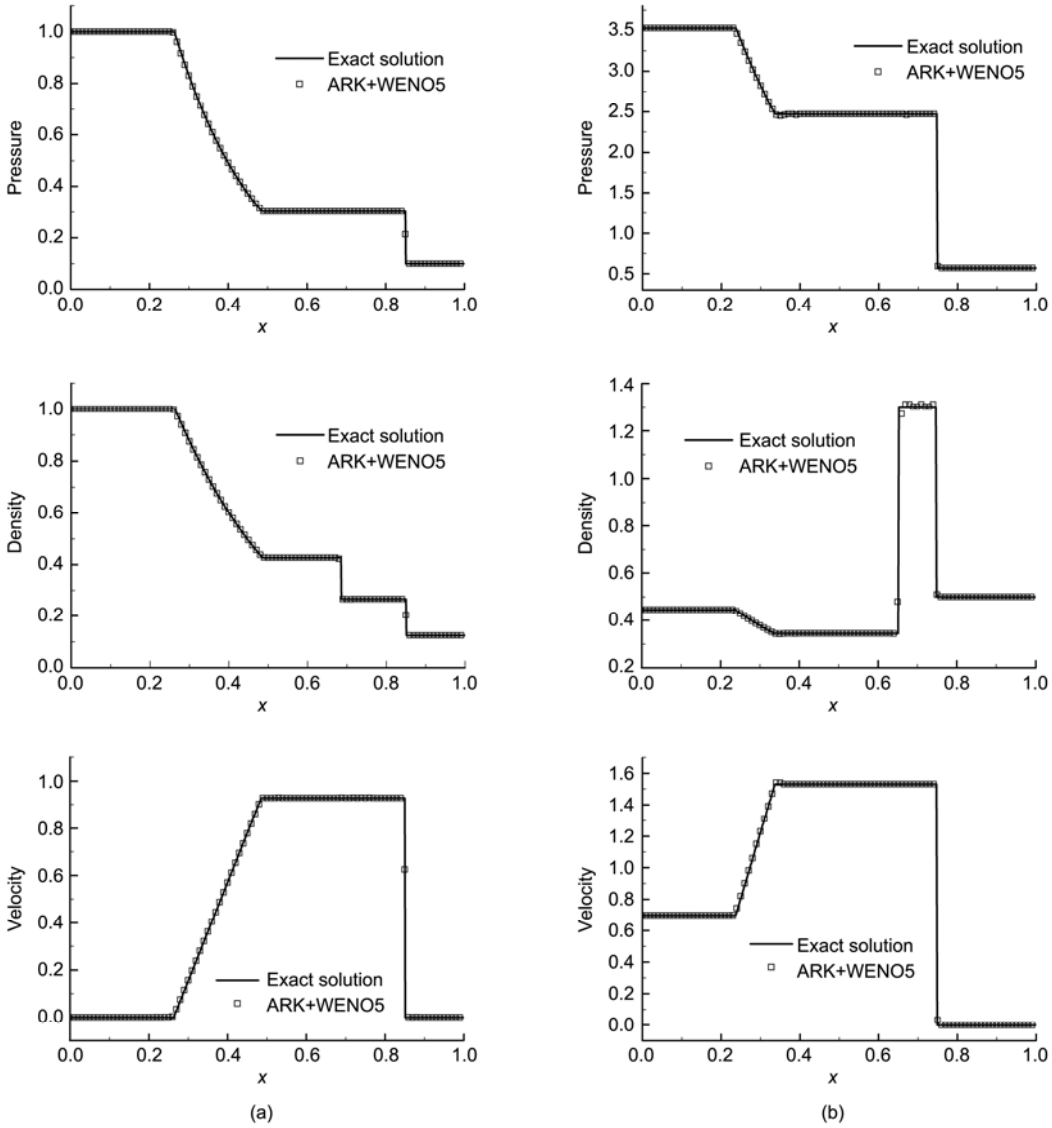

Figure 4 Comparison of the computed solution with the exact solution. (a) Sod shock tube problem; (b) Lax shock tube problem.

in which Y_i, e_i, ω_i are the mole fraction, the internal energy, and the mass production rate of i-th species. The density is a constant and $p=\rho RT$.

The numerical performance of the proposed methods were compared with other reported ARK2 methods in the literature, including the (2,3,3), (3,4,3), and (4,4,3) methods of Ascher et al. [30], LIRK3 and LIRK4 due to Calvo et al. [31], a five-stage, 3(2) pair of Fritzen and Wittekindt (FW53) [32]. Figure 5 show some numerical results of pressure, temperature, temperature gradient and mole fraction of major species and minor species.

We define work as the number of implicit solves required for the integration without regard to Newton iteration count. On error versus work plots, the five stage methods of Ascher (4,4,3) and Fritzen FW53 are least efficient. LIRK3 is the least efficient of the four remaining methods on this particular problem, followed by Ascher (3,4,3). The most accuracy efficient methods are ARK3(2)4L[2]SA and Ascher (2,3,3), shown in Figure 6 compares Calvo LIRK4 and ARK4(3)6L[2]SA at stiffness extremes showing that ARK4 (3)6L[2]SA is not only more accurate but increasingly so as the stiffness is increased.

3 Results and discussion

3.1 One-dimensional detonation

The effects of grid size on detonation parameters were illustrated in one-dimensional gaseous detonation. The results are summarized in Table 3. The von-Neumann pressure and reaction zone length are shown in Figure 7 as a function of the grid size. It is clearly that some detonation parameters including the detonation velocity, the C-J pressure and the wall pressure were fairly insensitive to the grid size, while

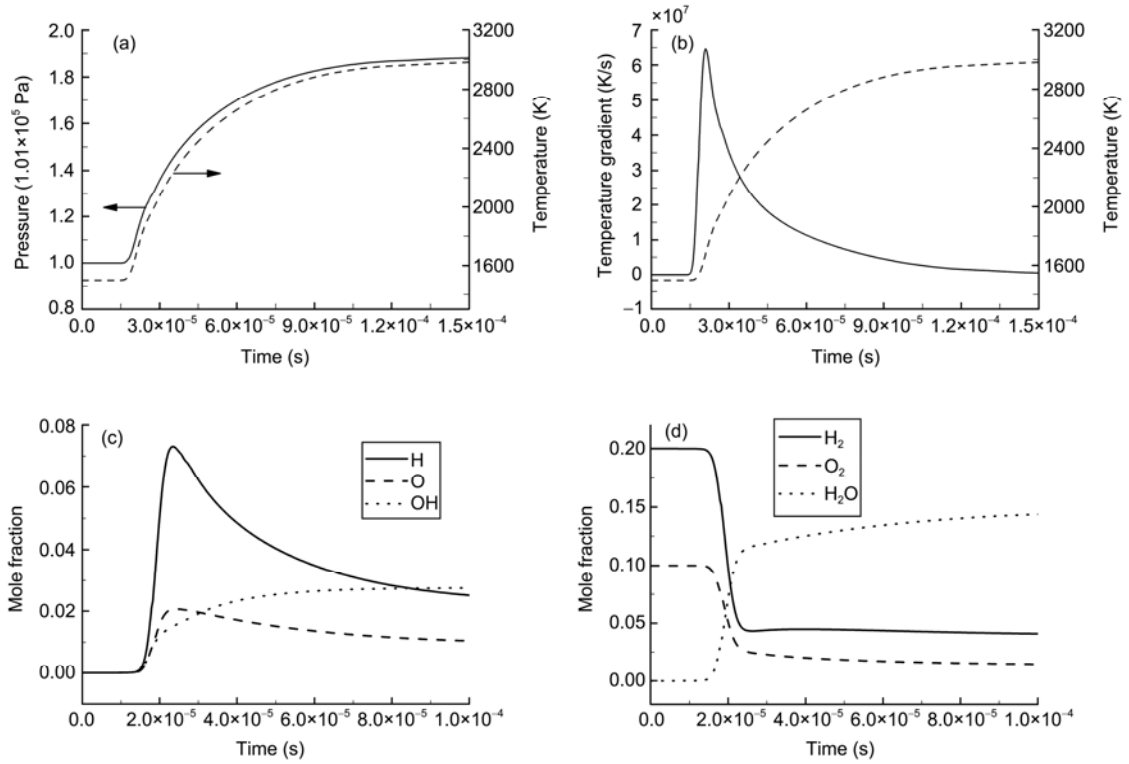

Figure 5 Profiles of CV structure for a stoichiometric mixture of hydrogen-argon. (a) Temperature and pressure; (b) temperature gradient and temperature; (c) minor species; (d) major species.

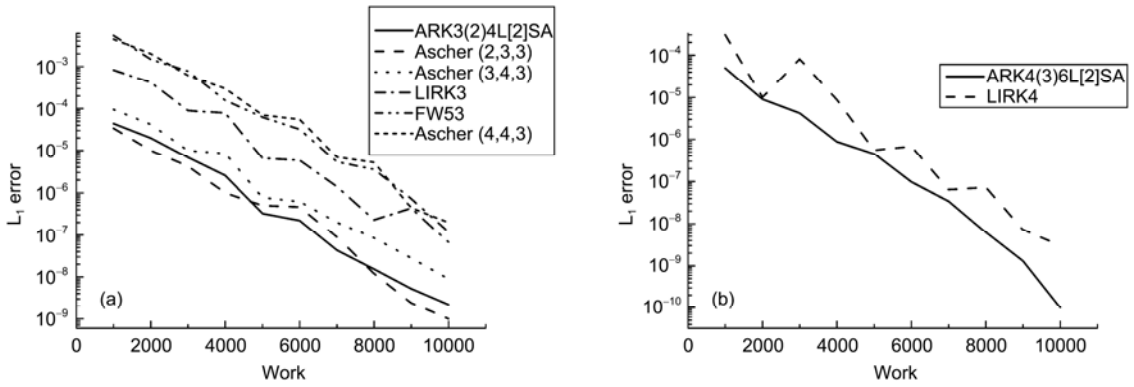

Figure 6 Error versus work for some IMEX Runge-Kutta methods. (a) Six third-order IMEX Runge-Kutta methods; (b) two fourth-order IMEX Runge-Kutta methods.

Table 3 Calculated detonation parameters with different grid sizes

Grid size (mm)	Detonation velocity (m/s)	C-J pressure (Pa)	Wall pressure (Pa)	V-N pressure (Pa)	Reaction zone length (mm)	Induction zone length (mm)
2	1620	93600	35830	135000	28	–
1	1620	93600	35830	149000	18	–
0.5	1620	93600	35830	159000	15	–
0.2	1620	93600	35830	166000	12	1.9
0.1	1620	93600	35830	169000	10	1.6
0.05	1620	93600	35830	172000	10	1.5

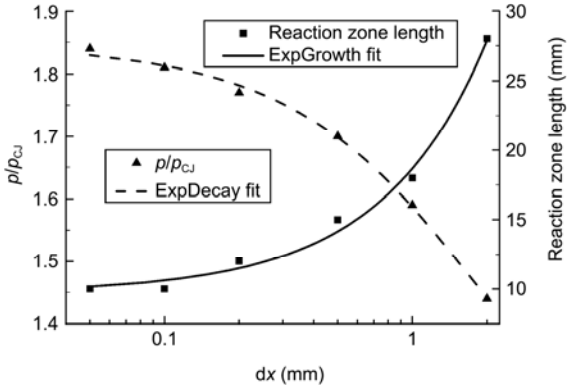

Figure 7 Peak pressure and reaction zone length versus grid size.

other parameters such as von-Neumann pressure, the reaction zone length and the induction zone length changed obviously as the grid size varied.

Both p/p_{CJ} and L_{rea} can be fit well by an exponential growth model:

$$p/p_{CJ} = 0.59158\, e^{\frac{-\Delta x}{1.73260}} + 1.25463,$$
$$L_{rea} = 282.632\, e^{\frac{-\Delta x}{32.1159}} - 272.603, \quad (25)$$

where L_{rea} refers to the reactive zone length, and Δx is grid size on space. When $\Delta x \to 0$, p/p_{CJ} and L_{rea} converge to 1.85 and 10 mm, respectively.

Some computed solutions are compared with other works in Table 4. The minimum induction zone length was found to be 15 mm in the present computations, which is pretty close to the result (0.147 cm) by Joseph et al. [33] while a little small than the result (0.16 cm) by Qu [34]; nevertheless, much larger than the reported value (2.0×10^{-3} cm)by Oran et al. [35].

3.2 Two-dimensional detonation

The triple wave configuration in the computed detonation front is shown in Figure 8. A typical triple wave configuration consists of the Mach stems, the incident waves and transverse waves, all intersect at the so-called triple points. As shown in Figures 8 and 9, the pressure and the density showed a peak around the triple points as a result of the collision between two neighboring transverse waves as the detonation wave propagated. The incident waves were wider while less intensive than the Mach stems, and meanwhile the gradients of pressure and temperature behind the incident waves were smaller than those behind the Mach stems. It indicates that the thermal chemistry reactions behind the incident waves fell behind those after the Mach stems. In addition, right at the Mach stems, the pressure and density distributions were not uniform and showed a trough in the middle.

Smoke-Foil Record of Detonation is a popular method for recording a detonation-wave structure involves the use of smoke-coated walls. As the detonation wave propagates, the high pressure generated at the shock-shock or shock-wall interaction point scratches the smoke-leaving a trace of the path of the high-pressure point on the wall. Propagation

Table 4 Comparison of the computed solution with other works for the 1D detonation wave

	This paper	Gordon [36]	Shepherd [33]	Oran [35]	Qu [34]
D_{CJ} (m/s)	1620	1618			1625
L_{ind} (m)	1.5×10^{-3}		1.47×10^{-3}	2.0×10^{-5}	1.6×10^{-3}
L_{rea} (m)	1.0×10^{-2}			1.2×10^{-2}	1.1×10^{-2}
V-N Pressure ($/p_{CJ}$)	1.85				1.79

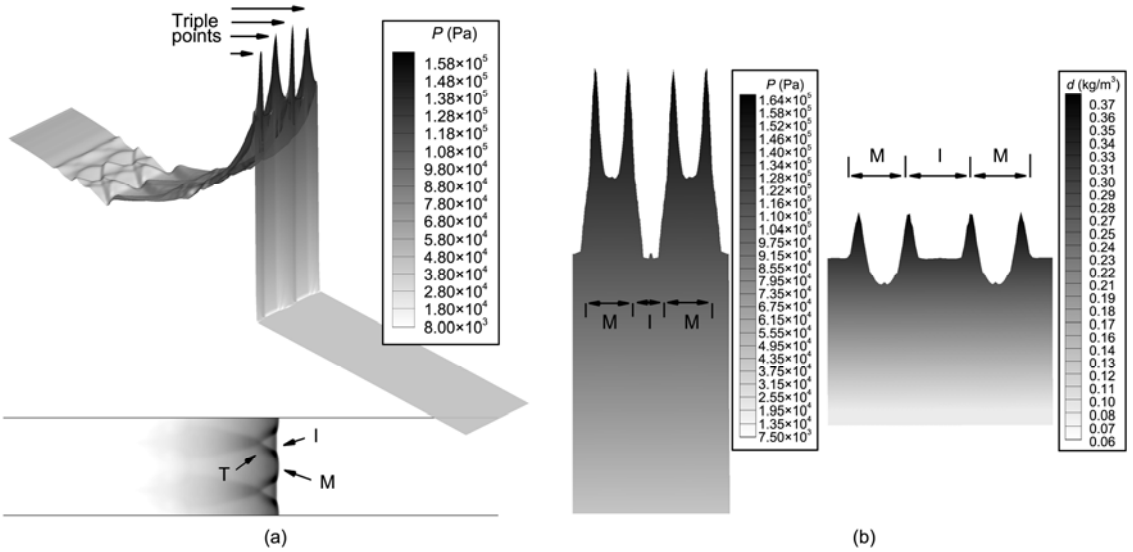

Figure 8 Detonation wave configuration. (a) Detonation front; (b) profiles of mach stem and incident along detonation front. M, Mach stem; I, Incident wave; T, Transverse wave.

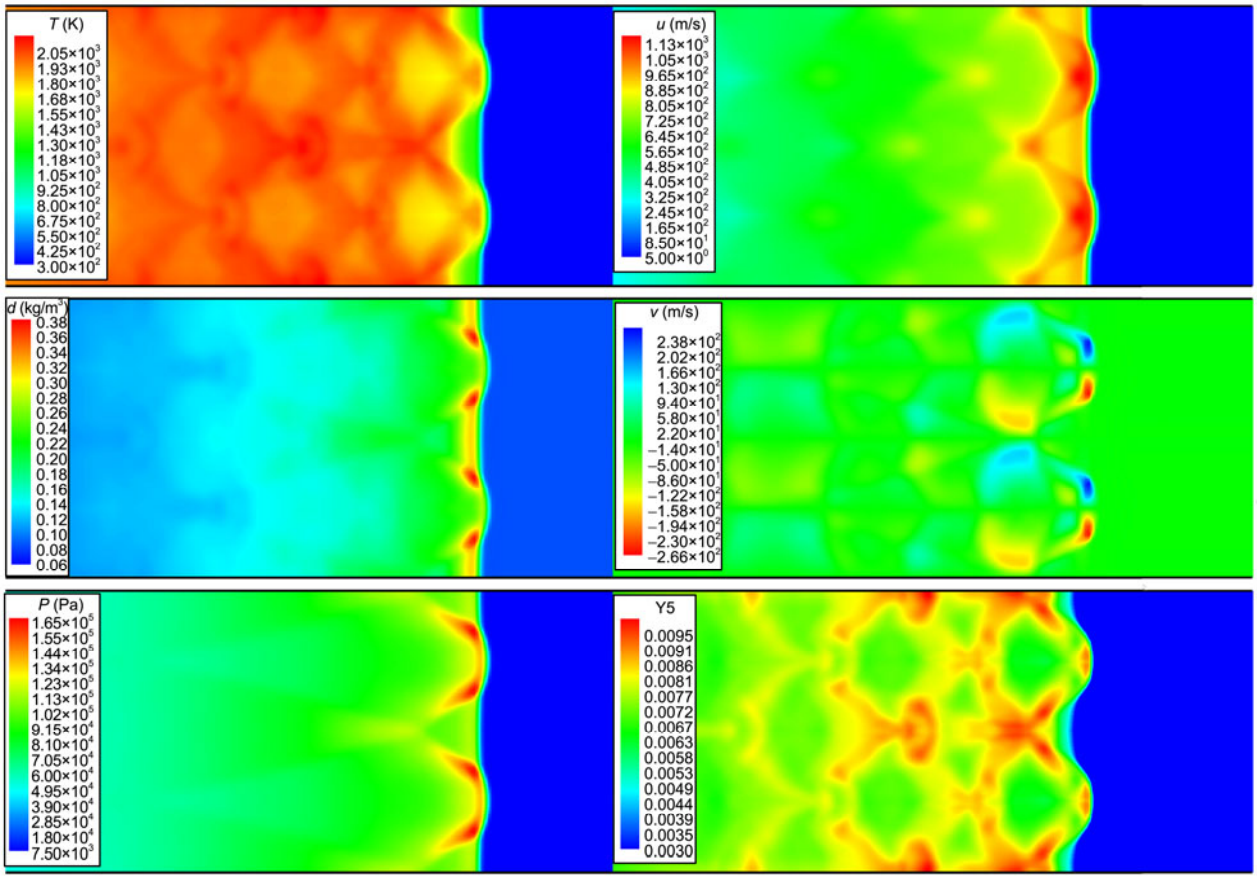

Figure 9 Profiles of pressure, density, temperature, velocity and mass fraction of OH.

of a detonation wave captured by the smoke-foil technique is shown here. The detonation wave was propagating in a channel from right to left. The fuel/air mixture was doped with tracer particles. As the detonation passed through, it scratched the smoke foil and displaced the particles. This technique has been used widely to study the tracks of the cellular structure experimentally (Figure 10(a)) and numerically (Figure 10(b)). Similarly, in the present work, the maximum mechanical power, $\Omega_{\max}$, on all grids in the time history were recorded to simulate the smoke foil tracks:

$$\Omega_{\max,i,j}=\left[\left(p\sqrt{u^2+v^2}\right)_{i,j}\right]_{\max},\quad t=0-t_{\text{end}}. \tag{26}$$

Figure 11 shows the pressure profiles at six different times points for the 2-D detonation wave is propagating in a 10 mm wide channel. The grid size was 0.2 mm. A fairly regular cellular structure with six transverse waves was observed, which was believed to be caused by the simultaneous presence of transverse waves, Mach stems and incident waves. Particularly, as the detonation wave propagated, the neighboring transverse waves collided with each other, and then led to the formation of new triple wave structures.

Figure 12 shows some characteristic parameters of the cellular pattern, including exit angle α, the radio of cell width to cell length λ/l, entrance angle β and angle of transverse wave trace ω. Parameters comparison listed in Table 5 show that the computed cells solution agrees well with experiment ones in quantity.

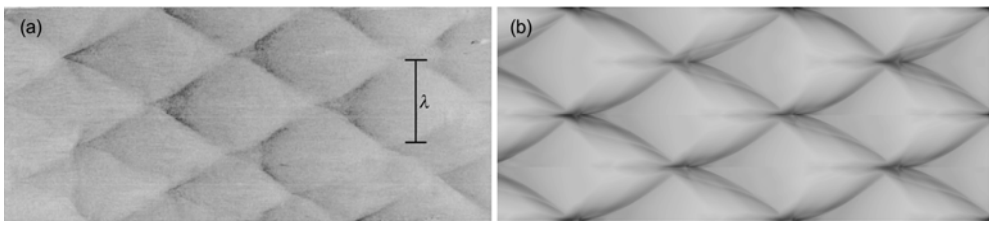

Figure 10 Detonation cellular pattern. (a) Experimental cellular pattern (Shepherd); (b) produced in numerical simulations.

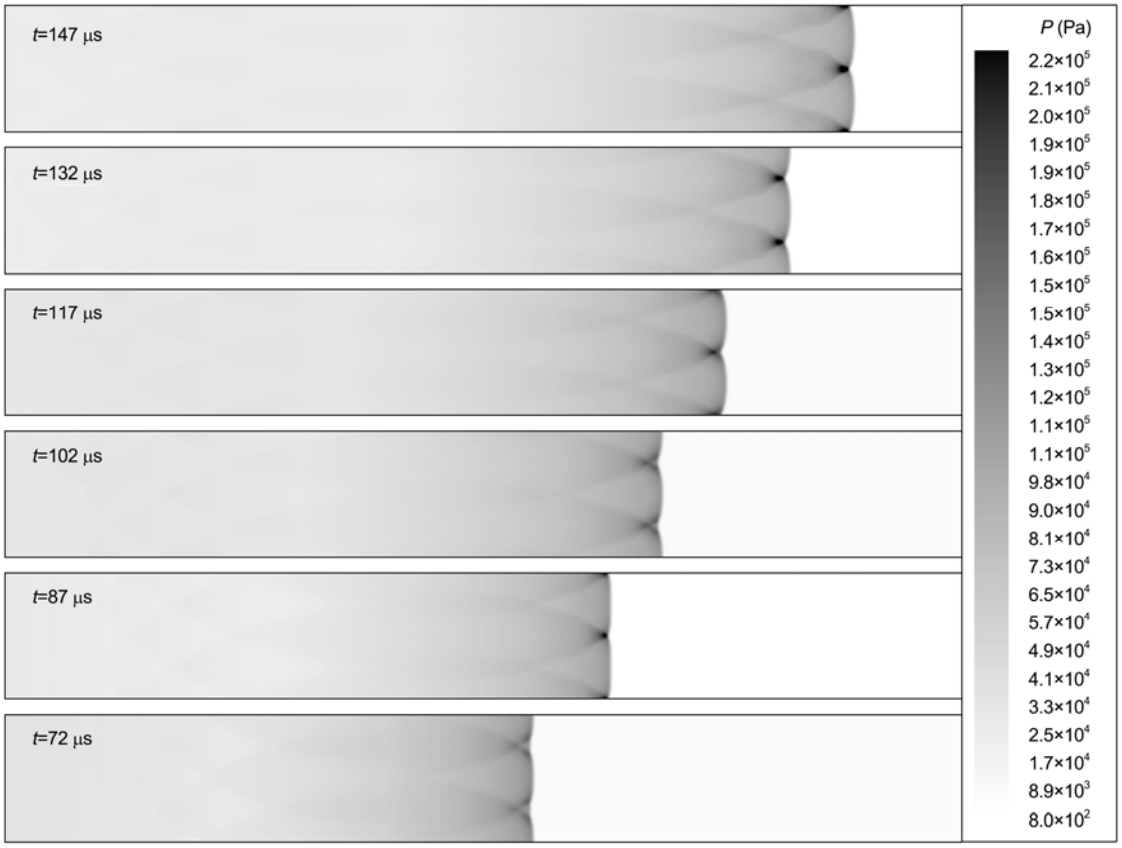

Figure 11 Simulated detonation wave propagation profiles at six time points.

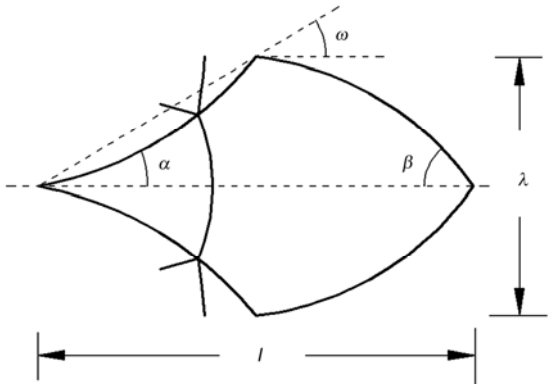

Figure 12 Some characteristic parameters of the cellular pattern.

Table 5 Parameters comparison of the computed cells solution with experiment ones

Cell structure parameters	Computation results	Experiment results [37,38]
λ/l	0.6	0.5–0.6
α	10	5–10
β	35–42	32–40
ω	~32	~30

3.3 Mach reflection of cellular detonations

Reflection of cellular detonation wave on a wedge has become increasingly important in the last decade due to its application in supersonic propulsion and relating interactions between cellular detonation wave and structure. In this section, we simulated Mach reflection of cellular detonations and captured cellular patterns on a wedge with a 19.3° angle.

Figure 13 shows the cellular patterns observed in experiment [39] and numerical results with the detailed chemical model using CE/SE scheme [40], TVD Runge-Kutta scheme, ARK scheme, respectively. It is found that there is a sharp dividing line emerging near the wedge and extending downstream. The size, shape and number of cells between the triple-point trajectory and the wedge are obviously different. From Figure 14, it is appropriate to say that the reflection on the wedge occurs in Mach reflection mode and that the dividing line denotes a triple-point trajectory (the black dash line). The case of Mach reflection of cellular detonations indicates that the ARK scheme can simulate cellular structure and reflection of gaseous detonations accurately.

Figure 15 shows three profiles of detonation cell pattern in the bend with bending angle θ=30°, 60° and θ=90°. There is a clearly visible difference in detonation cell pattern. In the bend, upper half is diffraction zone and lower half is mach reflection half. It is well known from the previous researches that mach reflection of detonation occurs depending on whether the wedge angle is less than critical

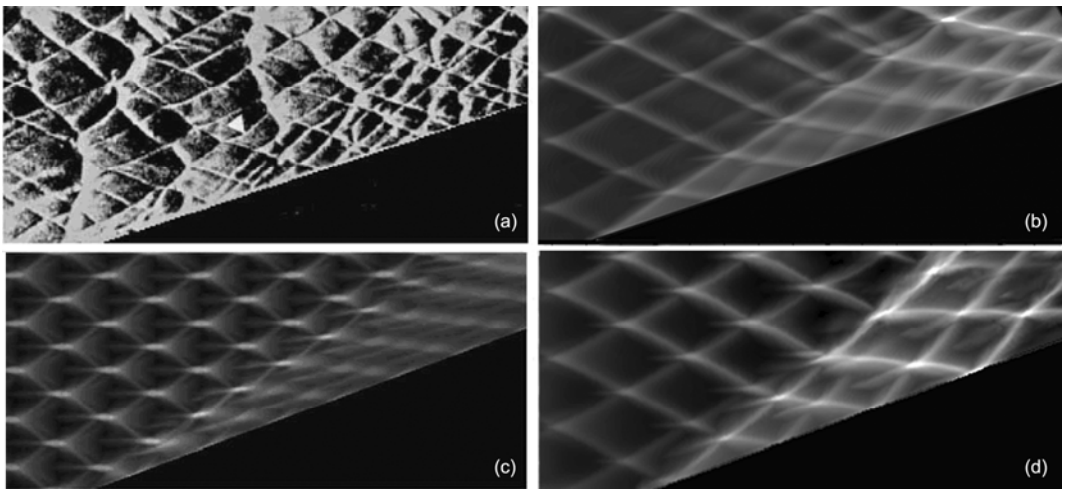

Figure 13 Cellular pattern produced in numerical simulations. (a) Experiment [39]; (b) detailed chemical reaction model and 3 order TVD Runge-Kutta scheme (this paper); (c) detailed chemical reaction model and CE/SE scheme [40]; (d) detailed chemical reaction model and 3 order ARK scheme (this paper).

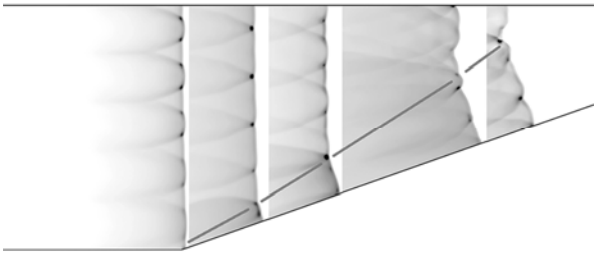

Figure 14 Cellular pattern produced in numerical simulations.

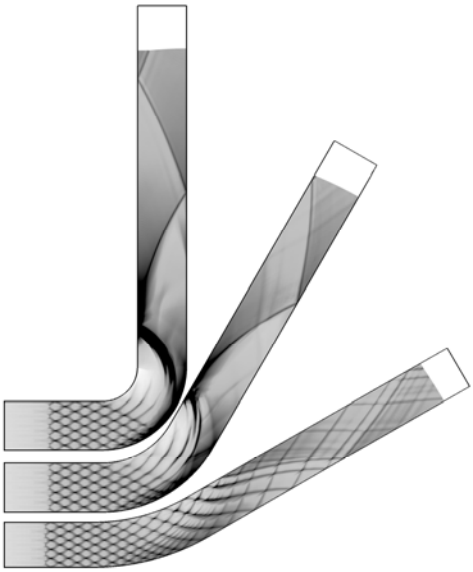

Figure 15 Cellular patterns produced in numerical simulations on smooth tube with bending angle 30°, 60° and 90°.

angle θ_c. According to Qu's work [34], in a stoichiometric H_2/O_2 mixture diluted with 70% argon at an initial pressure and temperature of 6.67 kPa and 298 K, θ_c=46°. A curve can be seen as a combination of many short straight lines; with the same reason, a concave surface of bend also could be thought as a combination of many wedges with angle increasing. Therefore a conclusion can be got that mach reflection occurs on outer wall at the very beginning until the turning point located at the cross section 46° from bend inlet. In Figure 15, we can found that the detonation cells pattern near the outer wall is regular and a little smaller than that in the initial section when the radius angle of concave surface is less than 46°, then becomes more irregular and disappears with the radius angle of concave surface is greater than 46°. The triple point trajectories under the reflected main triple point trajectory are convergent; in other words, the angle of the triple point trajectories near the outer wall is increasing behind the reflected mach stem. This is evidently different from detonation reflection from a wedge, in which the triple point trajectories are parallel with each other except the reflected main triple point trajectory behind the reflected mach stem.

4 Conclusions

The reactive Euler equations with a stiff source term were numerically solved using ARK_2 methods. The source term was resolved into a stiff part and a non-stiff part, in which the stiff part was solved explicitly while the non-stiff part was handled in an implicit way. A high numerical accuracy along with the L-stability can be achieved by using ARK_2 methods. The proposed methods and other methods reported in the literature were evaluated by numerically solving several test problems including the 2-dimensional detonation. Particularly, the proposed methods can reproduce the cellular pattern that has been observed experimentally. The results showed: (1) The numerical errors of the implicit and explicit Runge-Kutta methods were comparable when solving a equation with an intermediate stiffness; however, the im-

plicit method demonstrated a better numerical performance as the equation stiffness increases. (2) The stiffly accurate additive Runge-Kutta methods can capture the discontinuity well and describe the detonation complex wave configurations exactly, specially the typical characteristics such as triple wave structure, cellular cell, diffraction, reflection.

This work was supported by the National Basic Research Program of China (*2010CB832706*) *and National Natural Science Foundation of China* (*11032002, 11172045*).

1 Zhong X L. Additive semi-implicit Runge-Kutta methods for computing high-speed no equilibrium reactive flows. J Comput Phys, 1996, 128: 19–31
2 Ahmad S, Yue B Z. Impact of slip boundary on sloshing motions in partially filled containers. Chin Sci Bull, 2011, 56: 2674–2678
3 Hu S M, Tian Q Z, Xiao C, et al. A new detontion model and its examination by experiment (in Chinese). Sci Sin Phys Mech Astron, 2011, 41: 1230–1238
4 Yanenko N N. The Method of Fractional Steps. New York/Berlin: Springer-Verlag, 1971
5 Oran E S, Boris J P. Numerical Simulation of Reactive Flow. New York: Elsevier Science, 1987
6 Ma T B, Wang J, Ning J G. A hybrid VOF and PIC multi-material interface treatment method and its application in the penetration. Sci China Ser G-Phys Mech Astron, 2009, 39: 1185–1194
7 Fei G L, Ma T B, Hao L. Large-scale high performance computation on 3D explosion and Shock problems. Appl Math Mech-Engl Ed, 2011, 32: 375–382
8 Zhuang Z, Maitireyimu M. Recent research progress in computational solid mechanics. Chin Sci Bull, 2012, 57: 4683–4688
9 Hu X Y, Zhang D L, Jiang Z L. Numerical simulation of gaseous detonation with a detailed chemical reaction model. Acta Aerodyn Sin, 2003, 21: 59–66
10 Kennedy C A, Carpenter M H. Additive Runge-Kutta schemes for convection-diffusion-reaction equations. Appl Numer Math, 2003, 44: 139–181
11 Xia Y, Xu Y, Shu C W. Efficient time discretization for local discontinuous Galerkin methods. Discrete Cont Dyn-B, 2007, 18: 677–693
12 Wang C, Zhang X X, Shu C W, et al. Robust high order discontinuous Galerkin schemes for two-dimensional gaseous detonations. J Comput Phys, 2012, 231: 653–665
13 Fedkiw R P, Merriman B, Osher S. High accuracy numerical methods for thermally perfect gas flows with chemistry. J Comput Phys, 1997, 132: 175–190
14 Stall D R, Prophet H. JANAF Thermochemical Tables. 2nd ed. Washington: U. S. National Bureau of Standards, 1971
15 Wilson G J, MacCormack R W. Modeling supersonic combustion using a full-implicit numerical method. AIAA J, 1992, 30: 1008–1015
16 Araújo A L, Murua A, Sanz-Serna J M. Symplectic methods based on decompositions. SIAM J Numer Anal, 1997, 34: 1926–1947
17 Ning J G, Ren H L, Fang M J. A constitutive model based on the evolution and coalescence of elliptical micro-cracks for quasi-brittle materials. Chin Sci Bull, 2012, 57: 3773–3781
18 Alexander R, Coyle J J. Runge-Kutta methods and differential-algebraic systems. SIAM J Numer Anal, 1990, 27: 736–752
19 Hosea M E, Shampine L F. Analysis and implementation of TR-BDF2. Appl Numer Math, 1996, 20: 21–37
20 Alexander R. Diagonally implicit Runge-Kutta methods for stiff ODEs. SIAM J Numer Anal, 1977, 14: 1006–1021
21 Hairer E, Wanner G. Solving Ordinary Differential Equations II, Stiff and Differential-Algebraic Problems. 2nd ed. Berlin: Springer-Verlag, 1996
22 Zhang Y J, Liu Y D, Zhang Z H, et al. Computation on deflagration of hydrogen air mixture inside a duct and induced shell response. Sci China Ser G-Phys Mech Astron, 2009, 39: 1173–1184
23 Jiang G S, Shu C W. Efficient implementation of weighted ENO schemes. J Comput Phys, 1996, 126: 202–228
24 Liu X D, Osher S, Chan T. Weighted essentially non-oscillatory schemes. J Comput Phys, 1994, 115: 200–212
25 Shu C W, Osher S. Efficient implementation of essentially non-oscillatory shock capturing schemes. J Comput Phys, 1988, 77: 439–471
26 Shu C W, Osher S. Efficient implementation of essentially non-oscillatory shock capturing schemes II. J Comput Phys, 1989, 83: 32–78
27 Wu K T, Hao L, Wang C, et al. Level set interface treatment and its application in Euler method. Sci China Ser G-Phys Mech Astron, 2009, 39: 1204–1213
28 Wang C, Ma T B, Lu J. Influence of obstacle disturbance in a duct on explosion characteristics of coal gas. Sci China Ser G-Phys Mech Astron, 2009, 39: 1248–1257
29 Yang G T. Computational explosion mechanics and related progress. Chin Sci Bull, 2011, 56: 3610–3613
30 Ascher U M, Ruuth S J, Spiteri R J. Implicit-explicit Runge-Kutta methods for time-dependent partial differential equations. Appl Numer Math, 1997, 25: 151–167
31 Calvo M P, de Frutos J, Novo J. Linearly implicit Runge-Kutta methods for advection-reaction-diffusion equations. Appl Numer Math, 2001, 37: 535–549
32 Fritzen P, Wittekindt J. Numerical solution of viscoplastic constitutive equations with internal state variables. Part I: Algorithms and implementation. Math Method Appl Sci, 1997, 20: 1411–1425
33 Khasainov B, Presles H N, Desbordes D, et al. Detonation diffraction from circular tubes to cones. Shock Waves, 2005, 14: 187–192
34 Qu Q, Khoo B C, Dou H S, et al. The evolution of a detonation wave in a variable cross-sectional chamber. Shock Waves, 2008, 18: 213–233
35 Oran E S, Weber J E, Stefaniw E I, et al. A numerical study of two-dimensional H_2-O_2-Ar detonation using a detailed chemical reaction model. Combust Sci Tech, 1998, 113: 147–163
36 Gordon S, McBride B J. Computer program for calculation of complex chemical equilibrium compositions, rocket performance, incident and reflected shocks, and Chapman-Jouguet detonation. NASA SP-273, 1976
37 Wang G, Wang J T, Liu K X. New numerical algorithms in SUPER CE/SE and their applications in explosion mechanics. Sci China Ser G-Phys Mech Astron, 2009, 39: 1214–1220
38 Hu X Y. On the structures of gaseous detonation waves. Postdoctoral Report. Beijing: The Institute of Mechanics, Chinese Academy of Sciences, 2001
39 Guo C M, Zhang D L, Xie W. The mach reflection of a detonation based on soot track measurements. Combust Flame, 2001, 127: 2051–2058
40 Wang G, Zhang D L, Liu K X, et al. An improved CE/SE scheme for numerical simulation of gaseous and two-phase detonations. Comput Fluids, 2010, 39: 168–177